JM PAPERS

Direct numerical simulation of Taylor–Couette flow with vertical asymmetric rough walls

Fan Xu[1,2]**, Jinghong Su**[3,4]**, Bin Lan**[1,2]**, Peng Zhao**[2,5]**, Yurong He**[1,†]**, Chao Sun**[3,4,†] **and Junwu Wang**[2,5,6,†]

[1]School of Energy Science and Engineering, Harbin Institute of Technology, Harbin 150001, PR China

[2]State Key Laboratory of Multiphase Complex Systems, Institute of Process Engineering, Chinese Academy of Sciences, P. O. Box 353, Beijing 100190, PR China

[3]Center for Combustion Energy, Key Laboratory for Thermal Science and Power Engineering of Ministry of Education, Department of Energy and Power Engineering, Tsinghua University, Beijing 100084, PR China

[4]Department of Engineering Mechanics, School of Aerospace Engineering, Tsinghua University, Beijing 100084, PR China

[5]School of Chemical Engineering, University of Chinese Academy of Sciences, Beijing 100049, PR China

[6]Innovation Academy for Green Manufacture, Chinese Academy of Sciences, Beijing 100190, PR China

Direct numerical simulations are performed to explore the effects of the rotating direction of the vertically asymmetric rough wall on the transport properties of Taylor–Couette (TC) flow, up to a Taylor number of $Ta = 2.39 \times 10^7$. It is shown that, compared with the smooth wall, the rough wall with vertical asymmetric strips can enhance the dimensionless torque Nu_ω. More importantly, at high Ta, clockwise rotation of the inner rough wall (where the fluid is sheared by the steeper slope side of the strips) results in a significantly greater torque enhancement compared to counter-clockwise rotation (where the fluid is sheared by the smaller slope side of the strips), due to the larger convective contribution to the angular velocity flux. However, the rotating direction has a negligible effect on the torque at low Ta. The larger torque enhancement caused by the clockwise rotation of the vertically asymmetric rough wall at high Ta is then explained by the stronger coupling between the rough wall and the bulk, attributed to the larger biased azimuthal velocity towards the rough wall at the mid-gap of the TC system, the increased turbulence intensity manifested by larger Reynolds stress and a thinner boundary layer, and the more significant contribution of the pressure force on the surface of the rough wall to the torque.

Key words: Taylor–Couette flow, turbulent convection, shear-flow instability

† Email addresses for correspondence: rong@hit.edu.cn, chaosun@tsinghua.edu.cn, jwwang@ipe.ac.cn

975 A30-1

1. Introduction

Turbulent flows with rough walls are ubiquitous in nature, and many engineering applications must contend with rough boundaries. The viscous length scales in the flow decrease with increasing Reynolds numbers and, eventually, every surface appears to be rough, even when the roughness is small in absolute scale. Nikuradse (1933) was the first to study how local wall roughness (sand glued to the wall) affects global transport properties in pipe flow. Since then, numerous studies (Chan *et al.* 2018; Rouhi, Chung & Hutchins 2019; Ma *et al.* 2020; Modesti *et al.* 2021; Jelly *et al.* 2022) and reviews (Flack & Schultz 2014; Chung *et al.* 2021) have explored the effects of wall roughness in (pipe or channel) turbulence. Instead of using open-channel or pipe flow with rough walls, we employ a Taylor–Couette (TC) apparatus, which is a closed system with an exact balance between energy input and dissipation. Furthermore, due to its simple geometry and excellent controllability, the TC system offers favourable conditions for both numerical and experimental investigations (Verschoof *et al.* 2018; Zhu *et al.* 2018*b*).

In most experimental and numerical studies, both the inner and outer cylinders of the TC system are smooth surfaces (see Grossmann, Lohse & Sun (2016) for a comprehensive review). The effects of rough walls have only been investigated in recent decades. According to the shape of rough walls, they can be divided into three categories. The first type of rough wall is the irregular rough surface made by adhering particles randomly on the cylindrical wall (Berghout *et al.* 2019, 2021; Bakhuis *et al.* 2020). It was found that the torque can be enhanced by the irregular rough wall, indicating drag enhancement. The second type of rough wall is where the regular roughness is arranged in the way aligned with the mean flow, which is called 'parallel roughness'. It was found that the parallel grooves result in drag enhancement at relatively high Taylor numbers once the height of roughness is larger than the velocity boundary layer (BL) thickness (Zhu *et al.* 2016), which is because the plumes are ejected from the tips of these grooves and the system forms a secondary circulating flow inside the groove. Stronger plume ejections have an enhanced effect on the torque and then lead to drag enhancement. However, the parallel corrugated surface resulted in drag reduction at low Taylor number *Ta*, whereas drag enhancement was found at high *Ta* (Ng, Jaiman & Lim 2018; Razzak, Cheong & Lua 2020). Similar findings were also reported in studies employing micro-grooves (Razzak *et al.* 2020; Xu *et al.* 2023).

The third type is where the roughness is arranged perpendicular to the mean flow, i.e. 'vertical roughness'. Cadot *et al.* (1997) first reported this rough wall effect on drag by attaching vertical ribs on the inner and outer cylinders. Inspired by their work, Van den Berg *et al.* (2003) performed further experiments with the same style of roughness by conducting four groups of experiments, i.e. two smooth walls, rough-inner/smooth-outer, smooth-inner/rough-outer and two rough walls. Both studies found that the vertical roughness has a drag enhancement effect on the TC flow due to the extra torque of the rough elements coming from the pressure force. Zhu, Verzicco & Lohse (2017) carried out a quantitative analysis on the origins of torque at the rough wall and found that the contribution of pressure force to the torque at the rough wall is of prime importance for drag enhancement. Lee *et al.* (2009), Motozawa *et al.* (2013), Zhu *et al.* (2018*a*), Verschoof *et al.* (2018) and Sodjavi, Ravelet & Bakir (2018) also studied the effects of vertical rough walls, focusing on the effects of the number of vertical strips, the strip height and/or the radius ratio. To date, all studies on the effects of regular rough walls have used symmetrical, rough walls, resulting in the same influences by different rotating directions of the cylinders, whereas the asymmetric effect of different rotating directions
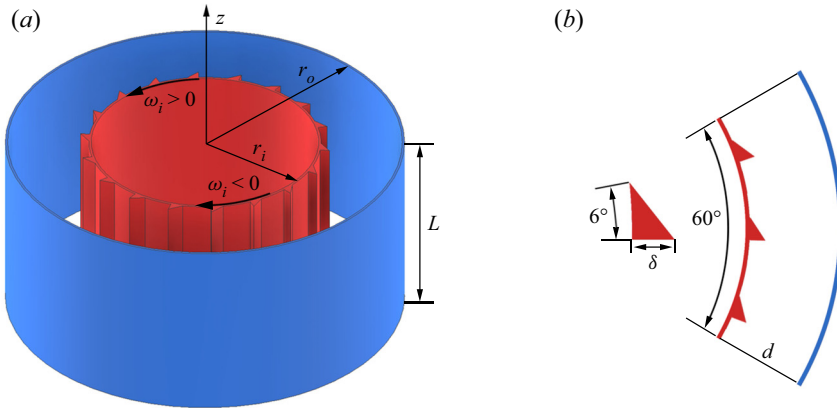
Figure 1. Schematic view of the Taylor–Couette system and the geometry of roughness. (*a*) Three-dimensional view. The inner cylinder with radius r_i is rotating with angular velocity ω_i. Here, $\omega_i > 0$ represents that the fluid is sheared by the smaller slope side of the strips, referred subsequently as counter-clockwise rotation; $\omega_i < 0$ indicates the fluid is sheared by the steeper slope side of the strips, referred subsequently as clockwise rotation. The outer cylinder with radius r_o is stationary. (*b*) Cross-section view of the gap between the two cylinders: $d = r_o - r_i$. The rough elements are eighteen triangular vertical strips positioned equidistantly on the inner cylinder wall. The height of the rough elements are $0.1d$ and $0.2d$. In the present simulations, a rotational symmetry of six is used. Therefore, the computational domain contains 1/6 of the azimuthal width and has three rough elements on the inner cylinder.

with vertical asymmetrical rough walls on the TC flow, which may make a huge difference, remains unexplored.

In this article, direct numerical simulation (DNS) of a TC flow with vertical asymmetrical rough walls is carried out to study how different rotating directions affect the global response as well as local flow behaviour. The manuscript is organized as follows. In § 2, the numerical method and settings are described. In § 3, the relationships between Nusselt number and Taylor number for vertical asymmetrical rough inner walls with different heights and rotating directions are presented, and the mechanism behind the differences in torque is explained. The local flow behaviour is also analysed. Finally, conclusions are drawn in § 4.

2. Numerical method and setting

In the present study, the outer cylinder is at rest, and the inner cylinder is rotating and thus driving the flow. The outer cylinder is a smooth wall and the inner one is a rough wall, with both walls subject to the no-slip boundary condition. Axially periodic boundary conditions are used, meaning that the present study does not include the effects of end walls presented in the TC experiments. The inner cylinder is roughened by attaching eighteen vertical strips of right triangle cross-section where one side of the strips is perpendicular to the inner wall and the strips with a height of δ are equally distributed in the azimuthal direction (see figure 1). The motivation behind this study is to investigate the impact of asymmetric roughness on torque in the Taylor–Couette system, particularly its effects on turbulent statistics. While there are various possibilities for asymmetric roughness shapes, we focus on the right triangular rib (the simplest asymmetric geometry model) as a starting point to examine the effects on statistics of turbulent Taylor–Couette flow. Our primary objective

is to investigate how the presence of asymmetric roughness elements impacts both global transport and local flow statistics in Taylor–Couette turbulence.

For the sake of simplicity and ease of explanation, as illustrated in figure 1(*a*), the angular velocity of the inner cylinder $\omega_i > 0$ represents that the fluid is sheared by the smaller slope side of the strips, referred subsequently as 'counter-clockwise rotation'. In contrast, $\omega_i < 0$ indicates the fluid is sheared by the steeper slope side of the strips, referred subsequently as 'clockwise rotation'. The gap width (d) is calculated as the difference between the radii of the outer cylinder (r_o) and the inner cylinder (r_i). The radius ratio is $\eta = r_i/r_o = 0.714$ and the aspect ratio is $\Gamma = L/d = 2\pi/3$, where L is the length of axial periodicity. The geometry of the system is fixed at the radius ratio of $\eta = 0.714$ and the outer cylinder is stationary, to make a direct comparison with previous results (Ostilla-Mónico *et al.* 2013; Xu *et al.* 2022). With $\Gamma = 2\pi/3$, we can have a relatively small computational domain with a pair of Taylor vortices. A rotational symmetry of six is selected to reduce the computational cost while not affecting the results, which has been verified by previous studies (Brauckmann & Eckhardt 2013; Ostilla-Mónico, Verzicco & Lohse 2015; Xu *et al.* 2022). As a result, there are only three triangular strips in the azimuthal direction, as shown in figure 1(*b*).

The fluid between the two cylinders is assumed to be Newtonian and incompressible. The motion of the fluid under these assumptions is governed by the continuity equation,

$$\nabla \cdot \boldsymbol{u} = 0, \tag{2.1}$$

and the momentum conservation equation (Zhu *et al.* 2016),

$$\frac{\partial \boldsymbol{u}}{\partial t} + \nabla \cdot (\boldsymbol{uu}) = -\nabla p + \frac{f(\eta)}{Ta^{1/2}} \nabla^2 \boldsymbol{u}, \tag{2.2}$$

where $\boldsymbol{u}$ and p are the dimensionless fluid velocity and pressure, respectively. The equations are normalized using the gap width d, and the tangential velocity of the inner cylinder $u_i = r_i\omega_i$, time is normalized by the characteristic length and velocity d/u_i, and the pressure term is normalized by the square of inner wall velocity and density ρu_i^2. We also define the non-dimensional radius r^* to be $r^* = (r - r_i)/d$. Here, $f(\eta)$ is a geometrical factor written in the form (Ostilla-Mónico *et al.* 2013; Zhu *et al.* 2016)

$$f(\eta) = \frac{(1 + \eta)^3}{8\eta^2}. \tag{2.3}$$

The Taylor number can characterize the driving TC flow. In the case of static outer cylinder, it is defined as (Grossmann *et al.* 2016)

$$Ta = \frac{(1 + \eta)^4}{64\eta^2} \frac{d^2(r_i + r_o)^2\omega_i^2}{\nu^2}, \tag{2.4}$$

where ν is the kinematic viscosity of the fluid. An alternative way to determine the system is using the inner Reynolds number that is defined as $Re_i = r_i\omega_i d/\nu$, and these two definitions can be interconverted using the formula $Ta = [f(\eta)Re_i]^2$. Both the Reynolds and Taylor numbers are presented in table 1. Moreover, the use of the Taylor number, instead of the Reynolds number, is common for distinguishing different TC flow regimes (Ostilla-Mónico *et al.* 2013, 2014*a*; Grossmann *et al.* 2016). In addition, we also provide the Reynolds number for the roughness based on the average azimuthal velocity at the height of the roughness, which is defined as $Re_\delta = \delta\bar{u}_{\varphi,r=r_i+\delta}/\nu$ and shown in table 1.

975 A30-4

δ/d	Ta	Re_i	Re_δ	$N_\varphi \times N_r \times N_z$	Nu_ω	$100\Delta_J$
0.1	1.87×10^3	-35	-3.25	$90 \times 90 \times 45$	1.08027	0.18
0.1	1.87×10^3	$+35$	$+3.25$	$90 \times 90 \times 45$	1.07885	0.22
0.1	4.61×10^3	-55	-5.19	$100 \times 100 \times 50$	1.09027	0.27
0.1	4.61×10^3	$+55$	$+5.18$	$100 \times 100 \times 50$	1.08859	0.25
0.1	1.06×10^4	-83.5	-7.94	$110 \times 110 \times 55$	1.09366	0.24
0.1	1.06×10^4	$+83.5$	$+7.93$	$110 \times 110 \times 55$	1.09224	0.31
0.1	3.90×10^4	-160	-14.49	$120 \times 120 \times 60$	2.04604	0.29
0.1	3.90×10^4	$+160$	$+14.45$	$120 \times 120 \times 60$	2.03780	0.25
0.1	1.03×10^5	-260	-22.63	$130 \times 130 \times 65$	2.68482	0.40
0.1	1.03×10^5	$+260$	$+22.56$	$130 \times 130 \times 65$	2.68105	0.36
0.1	2.44×10^5	-400	-33.51	$140 \times 140 \times 70$	3.37146	0.37
0.1	2.44×10^5	$+400$	$+33.40$	$140 \times 140 \times 70$	3.37098	0.41
0.1	7.04×10^5	-680	-55.53	$160 \times 160 \times 80$	4.48368	0.45
0.1	7.04×10^5	$+680$	$+55.20$	$160 \times 160 \times 80$	4.47725	0.42
0.1	1.91×10^6	-1120	-93.35	$200 \times 200 \times 120$	5.89129	0.57
0.1	1.91×10^6	$+1120$	$+92.87$	$200 \times 200 \times 120$	5.82758	0.54
0.1	3.90×10^6	-1600	-133.96	$230 \times 230 \times 150$	7.05058	0.66
0.1	3.90×10^6	$+1600$	$+132.35$	$230 \times 230 \times 150$	6.98768	0.71
0.1	9.52×10^6	-2500	-209.65	$250 \times 250 \times 200$	8.81297	0.79
0.1	9.52×10^6	$+2500$	$+206.55$	$250 \times 250 \times 200$	8.52065	0.72
0.1	2.39×10^7	-3960	-340.88	$320 \times 320 \times 250$	11.2194	0.80
0.1	2.39×10^7	$+3960$	$+336.40$	$320 \times 320 \times 250$	10.7176	0.85
0.2	1.87×10^3	-35	-6.51	$90 \times 90 \times 45$	1.27208	0.21
0.2	1.87×10^3	$+35$	$+6.50$	$90 \times 90 \times 45$	1.26989	0.20
0.2	4.61×10^3	-55	-10.52	$100 \times 100 \times 50$	1.27398	0.26
0.2	4.61×10^3	$+55$	$+10.51$	$100 \times 100 \times 50$	1.27167	0.28
0.2	1.06×10^4	-83.5	-16.18	$110 \times 110 \times 55$	1.27882	0.24
0.2	1.06×10^4	$+83.5$	$+16.14$	$110 \times 110 \times 55$	1.27699	0.21
0.2	3.90×10^4	-160	-29.68	$120 \times 120 \times 60$	2.36599	0.23
0.2	3.90×10^4	$+160$	$+29.57$	$120 \times 120 \times 60$	2.35736	0.26
0.2	1.03×10^5	-260	-44.34	$130 \times 130 \times 65$	3.18239	0.28
0.2	1.03×10^5	$+260$	$+44.09$	$130 \times 130 \times 65$	3.16564	0.31
0.2	2.44×10^5	-400	-69.03	$140 \times 140 \times 70$	4.08044	0.30
0.2	2.44×10^5	$+400$	$+68.40$	$140 \times 140 \times 70$	4.05339	0.32
0.2	7.04×10^5	-680	-116.07	$160 \times 160 \times 80$	5.56394	0.36
0.2	7.04×10^5	$+680$	$+114.57$	$160 \times 160 \times 80$	5.49542	0.33
0.2	1.91×10^6	-1120	-187.66	$200 \times 200 \times 120$	7.25148	0.41
0.2	1.91×10^6	$+1120$	$+185.92$	$200 \times 200 \times 120$	7.01813	0.45
0.2	3.90×10^6	-1600	-278.16	$230 \times 230 \times 150$	8.83068	0.49
0.2	3.90×10^6	$+1600$	$+271.54$	$230 \times 230 \times 150$	8.46703	0.47
0.2	9.52×10^6	-2500	-449.22	$250 \times 250 \times 200$	10.9950	0.58
0.2	9.52×10^6	$+2500$	$+439.74$	$250 \times 250 \times 200$	10.4784	0.59
0.2	2.39×10^7	-3960	-725.56	$320 \times 320 \times 250$	14.0615	0.69
0.2	2.39×10^7	$+3960$	$+712.28$	$320 \times 320 \times 250$	13.1831	0.73

Table 1. Values of the control parameters and the numerical results of the simulations. The columns display the strip height, the Taylor number, the inner Reynolds number, the Reynolds number for the roughness, the resolution employed, the dimensionless torque Nu_ω and the maximum deviation of angular velocity flux Δ_J, respectively. All of the simulations are run in reduced geometry with $\Gamma = 2\pi/3$ and a rotation symmetry of the order of six. The corresponding cases at the same Ta without roughness (with smooth cylinders) can be found in our previous study (Xu *et al.* 2022) and in that of Ostilla-Mónico *et al.* (2013).

In TC flow, the angular velocity flux from the inner cylinder to the outer cylinder is strictly conserved along the radius r (Eckhardt, Grossmann & Lohse 2007). It is defined as

$$J^\omega = r^3(\langle u_r\omega\rangle_{A,t} - \nu\partial_r\langle\omega\rangle_{A,t}), \tag{2.5}$$

where u_r is the radial velocity, ω is the angular velocity, and $\langle\dots\rangle_{A,t}$ denotes averaging over a cylindrical surface (averaging over the axial and azimuthal directions) with constant distance from the axis and over time. Here, the radius is selected to be within the scope of $r_i + \delta \leq r \leq r_o$. Additionally, J^ω is connected to the dimensionless torque Nusselt number Nu_ω via

$$Nu_\omega = J^\omega/J^\omega_{lam}, \tag{2.6}$$

where Nu_ω is the key response parameter in TC flow and $J^\omega_{lam} = 2\nu r_i^2 r_o^2 \omega_i/(r_o^2 - r_i^2)$ is the angular velocity flux of the non-vortical laminar state. Note that Nu_ω can be connected to the experimentally measurable torque τ via $\tau = 2\pi l\rho Nu_\omega J^\omega_{lam}$ by keeping the cylinder rotating with a constant velocity (Grossmann *et al.* 2016), where l is the height of the part of the cylinder on which the torque is measured and ρ is the fluid density.

Equations (2.1) and (2.2) are solved with a second-order-accuracy, colocated finite-volume method in the Cartesian coordinate system, using OpenFOAM as the computational platform. During the simulations, the results in the Cartesian coordinate are transformed to the format in the cylindrical coordinate, and the simulations are run for at least 40 large eddy turnover times $(d/r_i\omega_i)$ for data analysis. The no-slip boundary condition of the inner rough wall was dealt with a second-order-accuracy immersed boundary method (Zhao *et al.* 2020a,b). The temporal term is discretized using the second-order backward scheme and the convective term is discretized using a second-order total variation diminishing (Vanleer) scheme. All simulations are achieved using a fixed time step based on the Courant–Friedrichs–Lewy (CFL) criterion and the CFL number is less than 1.0 in all simulations. More details of the simulation accuracy are shown in Appendix A.

Two different strip heights ($\delta = 0.1d$ and $\delta = 0.2d$) on the inner cylinder with different rotating directions, i.e. $\omega_i > 0$ (counter-clockwise rotation) and $\omega_i < 0$ (clockwise rotation), were analysed. In each series with the same strip height, Ta ranges from 10^3 to 10^7 or Re_i is varied from 35 to 3960. The parameter space consists of the Taylor number Ta and the strip height δ/d, which are shown in figure 2. Note that the vertical solid lines in figure 2 are the transition values of Ta for smooth surfaces in TC flow, and the flow states are δ-dependent. The division of flow state is at a smooth surfaces and the radius ratio $\eta = 0.714$, which is in accordance with the classification methods proposed by Ostilla-Mónico *et al.* (2014a) and Grossmann *et al.* (2016), i.e. the determination of the critical Taylor number was based on the onset of Taylor vortices within the TC system.

3. Results

3.1. *Dimensionless torque*

To study the effect of the triangle strip walls, the dimensionless torque Nu_ω is presented as a function of Ta (i.e. $Nu_\omega = ATa^\beta$). Figure 3(a) shows the dimensionless torque Nu_ω with increasing Ta for a smooth wall and rough wall with two strip heights rotating in different directions. The results of previous smooth walls (Ostilla-Mónico *et al.* 2013) and parallel roughness walls (Zhu *et al.* 2016) are also shown in figure 3(a) for reference. In the non-vortical laminar flow regime, the flow only has an azimuthal velocity component and $Nu_\omega = 1$ for a smooth wall by definition. However, the values of Nu_ω are larger than 1
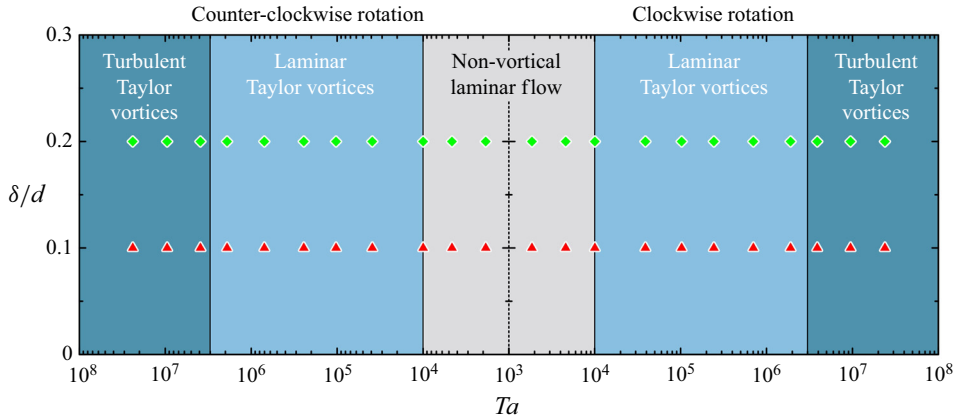
Figure 2. Explored (Ta, δ/d) parameter space. There are three different regimes in the phase spaces, i.e. the non-vortical laminar flow, the laminar Taylor vortices and the turbulent Taylor vortices regimes. The triangles represent the strip height of $0.1d$, the rhombuses show the strip height of $0.2d$.
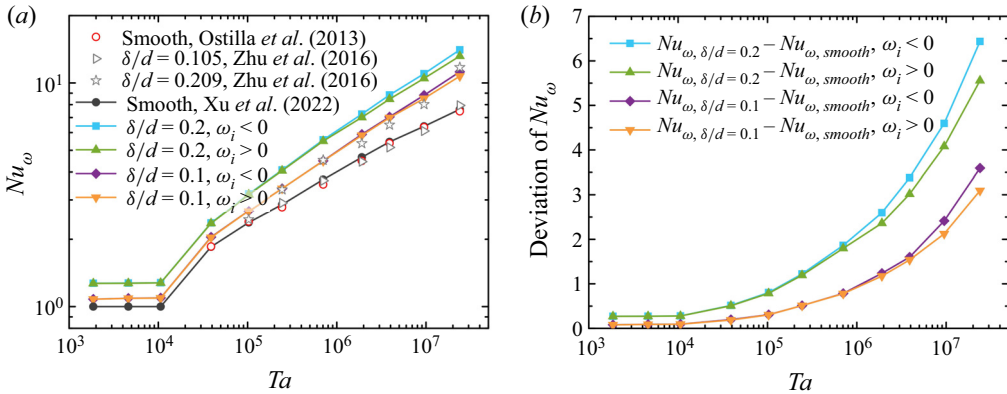

Figure 3. (*a*) Nusselt number as a function of Ta for smooth cases and rough cases with two strip heights for different rotating directions of the inner cylinder at $\eta = 0.714$. The results of previous smooth walls (Ostilla-Mónico *et al.* 2013; Xu *et al.* 2022) and parallel roughness walls with two different groove heights (Zhu *et al.* 2016) are also shown for reference. (*b*) The Nu_ω deviation between rough and smooth walls with increasing Ta.

for a rough wall, and a higher strip results in a larger Nu_ω. Although both flows for the smooth and rough cases are purely azimuthal at this regime, the ω-gradient of the latter is larger and the radial velocity $u_r = 0$. According to (2.5), the angular velocity flux J^ω for the rough walls is larger, i.e. the torque is larger. In addition, we also find that the critical Taylor number (Ta_c), determined based on the onset of Taylor vortices in the TC system, is affected by the rough surface. We conducted a series of simulations with various strip heights ($\delta = 0.1d$ and $\delta = 0.2d$) at different Taylor numbers. The critical Taylor number ($Ta_c \approx 1.15 \times 10^4$ or $Ta_c \approx 1.35 \times 10^4$) was identified as the value at which Taylor vortices became evident, while $Ta_c \approx 1 \times 10^4$ for a smooth wall in previous studies (Grossmann *et al.* 2016; Xu *et al.* 2022) with the same radius ratio $\eta = 0.714$, which means that the presence of a rough surface influences the value of this critical Taylor number. These results can be easily understood. The appearance of strips enlarges the effective radius of the inner cylinder, which makes the effective radius ratio of the
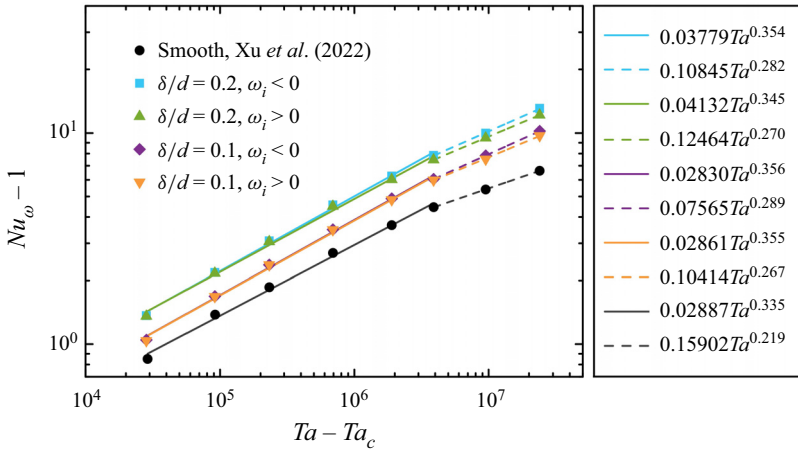
Figure 4. (*a*) Nusselt number as a function of *Ta* for smooth cases and rough cases with two strip heights for different rotating directions of the inner cylinder at $\eta = 0.714$. The data of rough cases are from the present study, and the data of smooth cases are from our previous study (Xu *et al.* 2022).

rough wall larger than that of the smooth wall, therefore, the critical Taylor number is larger (Pirro & Quadrio 2008).

After the onset of Taylor vortices, no matter whether walls are smooth or not, the torque Nu_ω increases with *Ta*. It is difficult to directly compare our results with other turbulent flow systems with rough walls, but the study with other types of rough walls in TC can be chosen for comparison. As shown in figure 3(*a*), despite the types of the roughness being discrepant, a similar conclusion is obtained, that is, higher roughness results in a larger torque. However, compared with the parallel roughness, the drag enhancement of the vertical one is better. In addition to this, the rotating direction of the rough inner cylinder has no effect on the torque at a fixed strip height for low Taylor numbers. This can be seen more clearly in figure 3(*b*), which presents the deviation of Nu_ω from the corresponding smooth one at different strip heights and rotating directions. It is shown that the effect of strip height on the torque becomes more significant with increasing *Ta* after the onset of Taylor vortices. Additionally, a higher strip results in a larger torque increase with the same Taylor number. In addition, the effects of rotating direction on the torque for different strip heights are different. For the case of $\delta = 0.2d$, the influence of rotating direction on torque appears when $Ta > 10^6$, and compared with the case of $\omega_i > 0$, the torque of $\omega_i < 0$ is larger. However, the effect of rotating direction on the torque comes out until $Ta \approx 10^7$ for $\delta = 0.1d$, and the difference between the counter-clockwise and clockwise rotations on the torque of $\delta = 0.1d$ is smaller than the corresponding difference of $\delta = 0.2d$ at the same *Ta*.

Here, $Nu_\omega - 1$ is the additional transport of angular velocity on the top of the non-vortical laminar transport in TC flow. Figure 4 shows the numerically calculated $Nu_\omega - 1$ with increasing *Ta* after the appearance of Taylor vortices. Here, we plot $Nu_\omega - 1$ versus $Ta - Ta_c$ rather than versus *Ta* to better show the scaling at low *Ta* (Ostilla-Mónico *et al.* 2013). For the smooth TC flow, from $Ta = 3.9 \times 10^4$ up to $Ta = 3 \times 10^6$, an effective scaling law of $Nu_\omega - 1 \sim (Ta - Ta_c)^{1/3}$ is found, which is connected with the laminar Taylor vortices regime. When $Ta > 3 \times 10^6$, there is a transitional region in which the bulk becomes turbulent but the large-scale coherent structure can still be identified when looking at the time-averaged quantities, which is associated with the turbulent Taylor
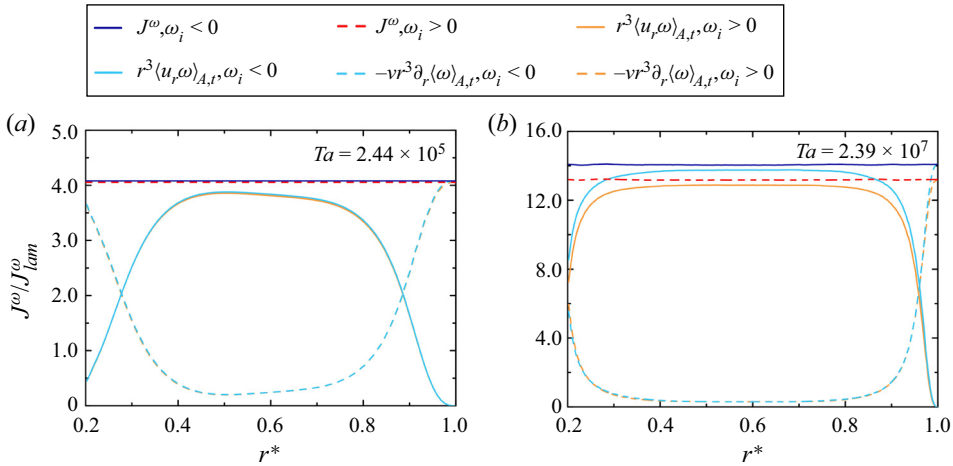
975 A30-8

Figure 5. Convective and diffusive contributions to the angular velocity flux for different rotating directions with $\delta = 0.2d$ at (*a*) $Ta = 2.44 \times 10^5$ and (*b*) $Ta = 2.39 \times 10^7$. All results are normalized by the angular velocity flux of the non-vortical laminar state J^{ω}_{lam}, and only the data within the scope of $r_i + \delta \leq r \leq r_o$ are shown.

vortices regime (Ostilla-Mónico *et al.* 2014*b*). In this transitional regime, the boundary layers are laminar first and become gradually turbulent with increasing *Ta*.

The situation becomes different for the TC flow with rough walls. As shown in figure 4, at the laminar Taylor vortices regime, the effective scaling exponent $\beta \approx 0.35$ for different strip heights on the inner cylinder ($\delta = 0.1d$ and $\delta = 0.2d$) rotating in clockwise ($\omega_i < 0$) and counter-clockwise ($\omega_i > 0$) directions. However, the situation becomes more complicated at the turbulent regime. The exponent β is influenced not only by the height of the strip, but also by the rotating direction of the inner rough wall. Figure 4 shows that the effect of strip height on the exponent does not show any regularity, but the influence of rotating direction of the inner rough wall is regular, i.e. the exponent β is slightly larger for the cases of $\omega_i < 0$ compared to the values of $\omega_i > 0$ at the same strip height.

In TC flow, the angular velocity flux is calculated as $J^{\omega} = r^3(\langle u_r \omega \rangle_{A,t} - \nu \partial_r \langle \omega \rangle_{A,t})$, where the first term is the convective contribution and the second term is the diffusive (or viscous) contribution (Eckhardt *et al.* 2007). The radial profiles of these two contributions for different rotating directions of the inner rough wall with $\delta = 0.2d$ at $Ta = 2.44 \times 10^5$ and $Ta = 2.39 \times 10^7$ are exemplified in figure 5. It can be seen that the convective contribution to the torque is mainly in the central region and disappears at the boundaries, as expected. In contrast, the diffusive contribution dominates near the walls but drops to almost zero in the middle.

Furthermore, as shown in figure 5(*a*), the rotating directions have no effect on the convective and diffusive contributions to J^{ω} at low Taylor number $Ta = 2.44 \times 10^5$ which is in the laminar Taylor vortices regime. However, as shown in figure 5(*b*), the situation becomes different at a large Taylor number $Ta = 2.39 \times 10^7$ that corresponds to the turbulent Taylor vortices regime. It can be seen that the diffusive contribution is still unaffected by the rotating direction of the inner rough wall except for the inner and outer boundaries, but the rotating direction has a significant effect on the convective contribution to the torque. When the inner wall rotates in the clockwise direction ($\omega_i < 0$), the convection term is larger than that of the counter-clockwise direction ($\omega_i > 0$).
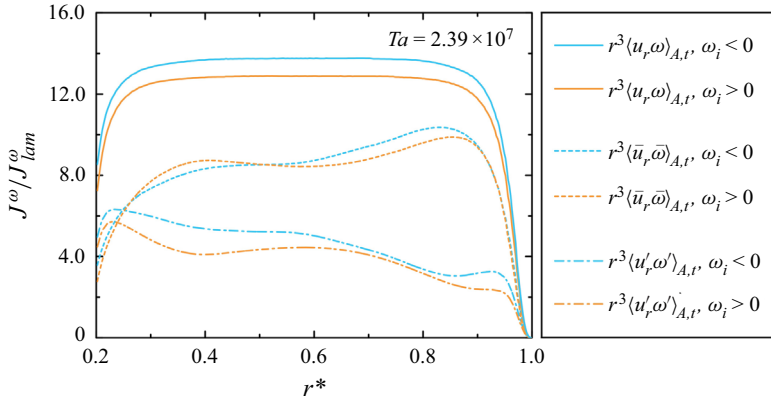
Figure 6. Average and fluctuation contributions to the convective term of total angular velocity flux for different rotating directions with $\delta = 0.2d$ at $Ta = 2.39 \times 10^7$. All results are normalized by the angular velocity flux of the non-vortical laminar state J_{lam}^{ω}, and only the data within the scope of $r_i + \delta \leq r \leq r_o$ are shown.

The results presented in figure 5 are consistent with those reported in figure 3 and show that the torque enhancement is dominantly due to the increased convective contribution.

To better explain why the rotating direction of the inner rough wall influences the convective term of torque at large Taylor number $Ta = 2.39 \times 10^7$ in figure 5(*b*), as shown in figure 6, the convection contributions to the total torque are further decomposed into two components: $r^3 \langle \bar{u}_r \bar{\omega} \rangle_{A,t}$ is the averages (which have a structure, due to the presence of Taylor rolls) and $r^3 \langle u_r' \omega' \rangle_{A,t}$ is arising from the correlation of the fluctuations. Figure 6 shows that compared with the turbulent convective flux $r^3 \langle u_r' \omega' \rangle_{A,t}$ caused by the Reynolds stress, the mean convective flux $r^3 \langle \bar{u}_r \bar{\omega} \rangle_{A,t}$ caused by the presence of mean Taylor vortices dominates to derive torques (Brauckmann & Eckhardt 2013). Additionally, when the rough inner wall rotates in different directions, for the average term, the value of clockwise rotation $\omega_i < 0$ near the smooth outer wall is greater than the value of counter-clockwise rotation $\omega_i > 0$, while the opposite is true on the side near the inner wall, which results in a small effect of the different rotation directions of the inner rough wall on the mean convective flux $r^3 \langle \bar{u}_r \bar{\omega} \rangle_{A,t}$ contribution to the total flux J^{ω}. However, the situation becomes simple for the fluctuant term, $r^3 \langle u_r' \omega' \rangle_{A,t}$ with $\omega_i < 0$ always greater than the value with $\omega_i > 0$ at the same radius, indicating that the turbulence caused by clockwise rotation ($\omega_i < 0$) is more intense than that of $\omega_i > 0$. Those facts lead to the observed torque enhancement and the different effects of rotating directions.

3.2. *The mechanism of torque enhancement*

To understand the mechanism underlying the torque enhancement and the effect of rotating directions, it is useful to analyse the dependence of the azimuthal velocity profiles $u_{\varphi}(r)$ on the driving parameter *Ta*. Therefore, $u_{\varphi}(r)$ for two representative Taylor numbers $Ta = 2.44 \times 10^5$ and $Ta = 2.39 \times 10^7$ are presented in figure 7. It can be seen that the azimuthal velocity profiles are influenced by the strip height, where a higher strip results in a larger azimuthal velocity at the same radius. For small Taylor number $Ta = 2.44 \times 10^5$, the azimuthal velocity profiles are almost unaffected by the rotating direction of the inner rough wall. At large Taylor number $Ta = 2.39 \times 10^7$, the rotating direction has an effect on the azimuthal velocity profiles, that is, the clockwise rotation $\omega_i < 0$ of the vertical
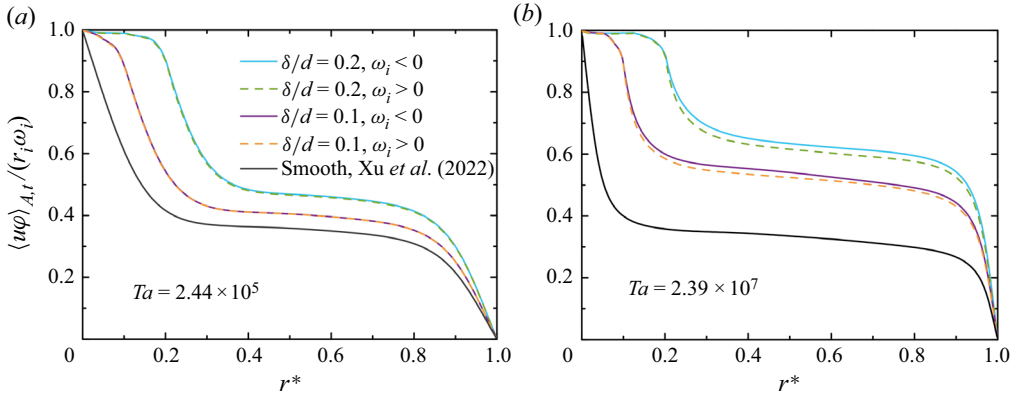
975 A30-10

Figure 7. Averaged azimuthal velocity profiles for different rotating directions of the inner rough wall with two strip heights at (*a*) $Ta = 2.44 \times 10^5$ and (*b*) $Ta = 2.39 \times 10^7$. The averaged azimuthal velocity profiles for smooth walls at these two Ta from our previous study (Xu *et al.* 2022) are also included for comparison.

asymmetric rough wall makes the azimuthal velocity larger at a given *r*, compared with the case of counter-clockwise rotation $\omega_i > 0$. This is because the shear rate of the azimuthal velocity at the rough wall is smaller than that in the corresponding smooth case (Van den Berg *et al.* 2003; Zhu *et al.* 2017), and the azimuthal velocity should be biased towards the rough wall at the mid gap compared with the smooth case, leading to the stronger coupling between the rough wall and the bulk. Furthermore, the difference in azimuthal velocity profiles with a higher strip height between counter-clockwise and clockwise rotation is larger. These observations explain the torque enhancement and the effects of rotating direction to a certain extent.

It is well known that the characteristics of velocity boundary layer (BL) reflect many features of wall turbulence (Grossmann *et al.* 2016). Therefore, the non-dimensionalized azimuthal velocity profiles u^+ versus the wall distance y^+ for the outer smooth wall and the inner rough wall in the case of $Ta = 2.39 \times 10^7$ are shown in figure 8. Figure 8(*a*) shows that there is a viscous sublayer ($u^+ = y^+$), which is well known for a smooth wall. The BL of the outer wall is influenced by the height of the strip attached to the inner wall, resulting in upward shifts of the log-law region, that is, a higher strip results in a larger shift. However, the rotating direction of inner rough wall with the same strip height has no effect on the characteristics of velocity boundary layer near the outer stationary wall. For the inner cylinder, it can be seen from figure 8(*b*) that the BL is not only influenced by the strip height, but also affected by the rotating direction of the inner wall. Compared with the smooth inner wall, significant downward shifts are acquired for the rough cases, which are similar to the results of Zhu *et al.* (2016). Meanwhile, the downward trend is larger for the higher strip or for clockwise rotation ($\omega_i < 0$) of the inner rough wall with the same strip height. It means that a higher strip and clockwise rotation ($\omega_i < 0$) of the inner rough wall can form a thinner BL at this Ta. As a result, the torque enhancement becomes more obvious with the higher strip and clockwise rotation of the inner rough wall at large Ta.

We also plot the dimensionless value δ/δ_v of the roughness height in wall units for different strip heights in figure 9, where the grey and blue dashed lines denote the boundaries of the viscous sublayer ($\delta/\delta_v < 5$) and buffer layer ($5 < \delta/\delta_v < 30$) (Pope 2000). Figure 9 shows that if these dimensionless values are in the viscous sublayer, the flow is dominated by viscous effects and the rotation direction of the asymmetric rough wall has no change at all on the torque Nusselt number (which can be seen in figure 3*b*),
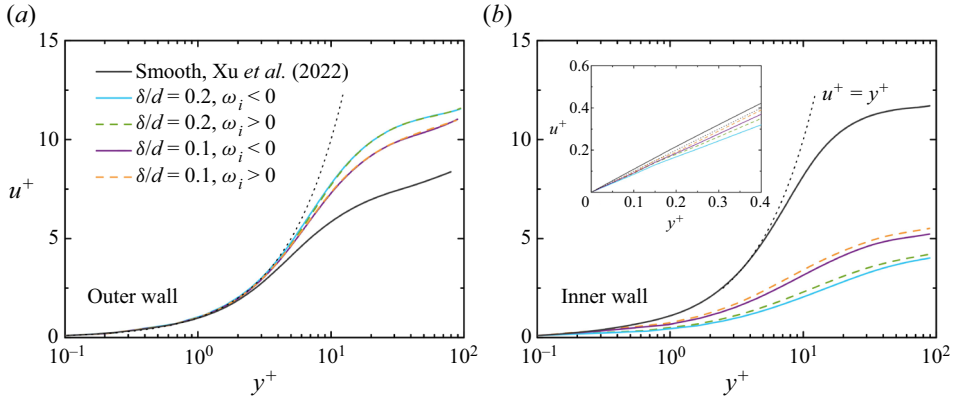
Figure 8. Non-dimensionalized azimuthal velocity profiles (*a*) for the outer stationary wall and (*b*) for different rotating directions of the inner rough wall with $\delta = 0.1d$ and $\delta = 0.2d$ versus wall distance at $Ta = 2.39 \times 10^7$. The inset in figure 8(*b*) is the enlargement near the inner wall. The non-dimensionalized azimuthal velocity profiles for a smooth wall at the same *Ta* are from our previous study (Xu *et al.* 2022). For the outer smooth wall, the non-dimensionalized azimuthal velocity profile is $u^+ = \langle u_\varphi \rangle_{A,t}/u_\tau$ and the wall distance is $y^+ = (r_o - r)/\delta_v$, where the friction velocity is $u_\tau = \sqrt{\tau/2\pi l\rho r^2} = \sqrt{Nu_\omega J_{lam}^\omega/r^2}$, the boundary layer thickness δ_v is estimated by $\delta_v \approx d\sigma/(2Nu_\omega)$, and σ is defined as $\sigma = [(r_i + r_o)/(2\sqrt{r_o r_i})]^4$ (Brauckmann & Eckhardt 2013; Zhu *et al.* 2017); for the inner rough wall, the non-dimensionalized azimuthal velocity profile $u^+ = (\bar{u}_{\varphi, r=r_i+\delta} - \langle u_\varphi \rangle_{A,t})/u_\tau$ and the wall distance $y^+ = (r - r_i - \delta)/\delta_v$. The dotted lines show the relationships $u^+ = y^+$.
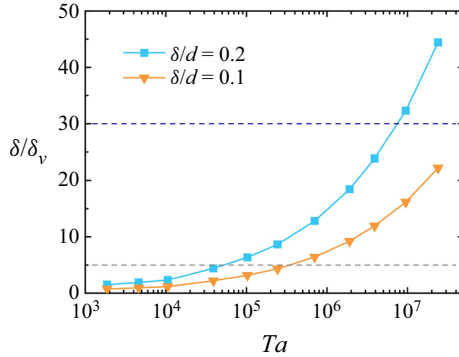

Figure 9. Dimensionless value of the roughness height δ in wall units. The grey and blue dashed lines denote the boundaries of the viscous sublayer ($\delta/\delta_v < 5$) and buffer layer ($5 < \delta/\delta_v < 30$).

which is similar to the common finding that the rough surface becomes active only when the thermal boundary layer thickness is smaller than the characteristic height of roughness (Shen, Tong & Xia 1996; Stringano, Pascazio & Verzicco 2006) in Rayleigh–Bénard (RB) flow. In TC flow with parallel grooves, the same results reported by Zhu *et al.* (2016) showed that the effect of grooves on the torque Nu_ω can only be seen when the BL thickness becomes thinner than the groove height. However, the pressure drag is affected by the rotation direction of the asymmetric roughness in the buffer layers when $\delta/\delta_v \approx 16$ for $\delta = 0.1d$ at $Ta = 9.52 \times 10^6$ and $\delta/\delta_v \approx 16$ for $\delta = 0.2d$ at $Ta = 1.91 \times 10^6$ in the present simulations (as shown in figure 10*b*). Furthermore, it is worth noting that a two-dimensional triangle with the top facing forward (into the wind) has a lower drag
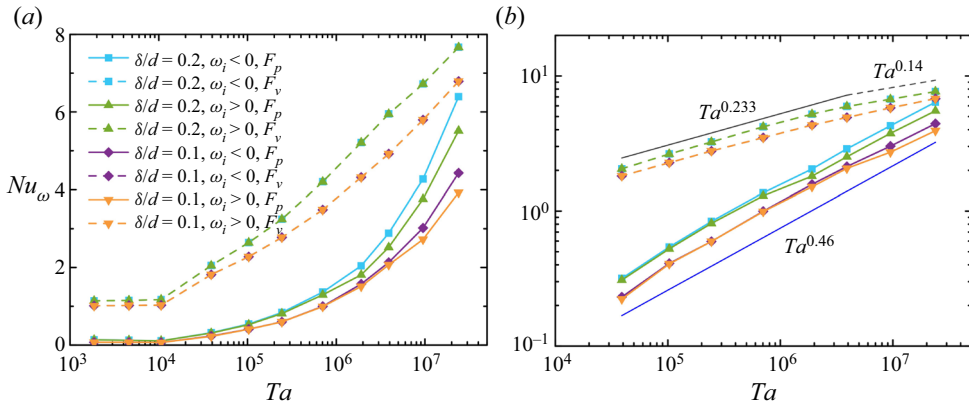
975 A30-12

Figure 10. (*a*) Contributions to the total torque originating from the pressure force Nu_p and the viscous force Nu_v with two strip heights $\delta = 0.1d$ and $\delta = 0.2d$ on the inner wall rotating in different directions. The solid lines represent the contribution of the pressure force F_p to the total torque, and the dash ones represent the contribution of the viscous force F_v. (*b*) Log-log scale of figure 10(*a*).

as compared with the same triangle with the top pointing in the downstream direction at sufficiently large Reynolds numbers (e.g. drag coefficient 1.6 versus 2.0 according to White, Fluid Mechanics, 2011, table 7.2). Our results are consistent with White (2011), albeit the Reynolds number is relatively lower and the triangles are attached to the wall.

In the present study, the TC system is driven by the rotation of the inner cylinder. To reveal the mechanism of torque enhancement more directly, it is necessary to study the torque at the inner wall. To find the mechanism behind the increase of Nu_ω for the vertical strips on the inner wall, the pressure and viscous contributions at the rough wall are quantified. The part of the pressure force is defined as (Zhu *et al.* 2017)

$$Nu_p = \int \frac{pr}{\tau_{pa}} \mathrm{d}S, \tag{3.1}$$

where *p* is the pressure, *r* is the radius, and τ_{pa} is the torque required to drive the system in the purely azimuthal and laminar flow. While the part of viscous force is defined as (Zhu *et al.* 2017)

$$Nu_v = \int \frac{\tau_v r}{\tau_{pa}} \mathrm{d}S, \tag{3.2}$$

where τ_v is the viscous shear stress.

Figure 10(*a*) shows the contributions to the total torque originating from Nu_p and Nu_v for an asymmetric vertical rough wall rotating in different directions with two strip heights $\delta = 0.1d$ and $\delta = 0.2d$, and the log-log scale is also shown in figure 10(*b*) at laminar and turbulent vortex regimes. As shown in figure 10(*a*), at small Taylor numbers, the torque on the rough wall almost all comes from the viscous force. With increasing *Ta*, the contributions of viscous and pressure forces to the torque both increase, but the latter is significantly faster than the former. More importantly, Nu_v is independent of the rotating directions at a same strip height although the strip is asymmetric. Furthermore, the higher the strip, the larger the viscous force to the total torque at the same *Ta*. By contrast, Nu_p in the clockwise rotation cases are larger than those for counter-clockwise rotation at the same strip height, which has not been seen in the previous study with symmetric rough walls (Zhu *et al.* 2017). Those facts explain the results shown in figure 3, that is, the torques of

clockwise rotation become larger than those of counter-clockwise rotation for the same *Ta* and indicate that the torque difference of different rotating directions is dominantly due to the different contribution of Nu_p.

Furthermore, we also plot the log-log scale in figure 10(*b*) from $Ta = 3.9 \times 10^7$ to $Ta = 2.39 \times 10^7$. This reveals that both the contribution of viscous forces to torque and the overall torque display segmented power-law relationships with respect to *Ta*. In both scenarios, distinct power-law exponents emerge in the laminar and turbulent Taylor vortex regimes. Within the laminar regime, the power-law exponent is greater, signifying a more pronounced dependency of torque contribution on *Ta*. Conversely, in the turbulent regime, the power-law exponent is smaller, indicating a comparatively weaker dependency. However, unlike the segmented power-law relationship between viscous forces and *Ta*, the contribution of pressure to torque does not exhibit a segmented power-law relationship with *Ta*. Instead, it is characterized by a smaller prefactor yet a larger power-law exponent. This suggests that pressure plays a more substantial role in torque generation, showing a stronger dependence on *Ta*. This implication aligns with the dominance of pressure at high Taylor numbers, as reported by Zhu *et al.* (2017). In summary, these observations indicate the intricate relationships between viscous stress and pressure in different *Ta* number regimes.

4. Conclusions

In the present study, extensive direct numerical simulations were conducted to explore the effect of inner rough walls on the transport properties of Taylor–Couette flow. The inner cylinder was roughened by attaching 18 vertical asymmetric strips, with strip heights of $\delta = 0.1d$ and $\delta = 0.2d$. Numerical results were obtained for *Ta* ranging from 1.87×10^3 to 2.39×10^7 at a radius ratio of $\eta = 0.714$ and an aspect ratio of $\Gamma = 2/3\pi$, using periodic boundary conditions in the azimuthal and axial directions.

The main conclusions that can be drawn include: (i) the rotation direction of the vertical asymmetric rough wall has a negligible effect on the torque at low Taylor numbers. The influence gradually becomes more pronounced with increasing *Ta*, and the drag enhancement effect of clockwise rotation of the inner cylinder is more significant than that of counter-clockwise rotation; (ii) the rotation direction of a vertical asymmetric rough wall also has a negligible effect on the azimuthal velocity and the Reynolds stress at low Taylor number, they are however larger at high *Ta* when the inner cylinder rotating in clockwise direction; (iii) for large *Ta*, the velocity boundary layer (BL) in the case of clockwise rotation is thinner than that in the case of counter-clockwise rotation, due to the observed stronger turbulence; (iv) the torque on the vertical asymmetric rough wall is derived from the viscous force and the pressure force. The contribution of the viscous force to the torque with the same strip height is always equal at the same *Ta*, irrespective of the rotating direction of the inner vertical asymmetric wall. However, the contribution of the pressure force to the torque for the same strip height is unaffected by the rotating direction of the inner wall at low Taylor numbers but is significantly affected at large *Ta*. Moreover, the contribution of the pressure force in the case of clockwise rotation is larger than that in the case of counter-clockwise rotation, resulting in the observed larger torque in clockwise rotation.

Declaration of interests. The authors report no conflict of interest.
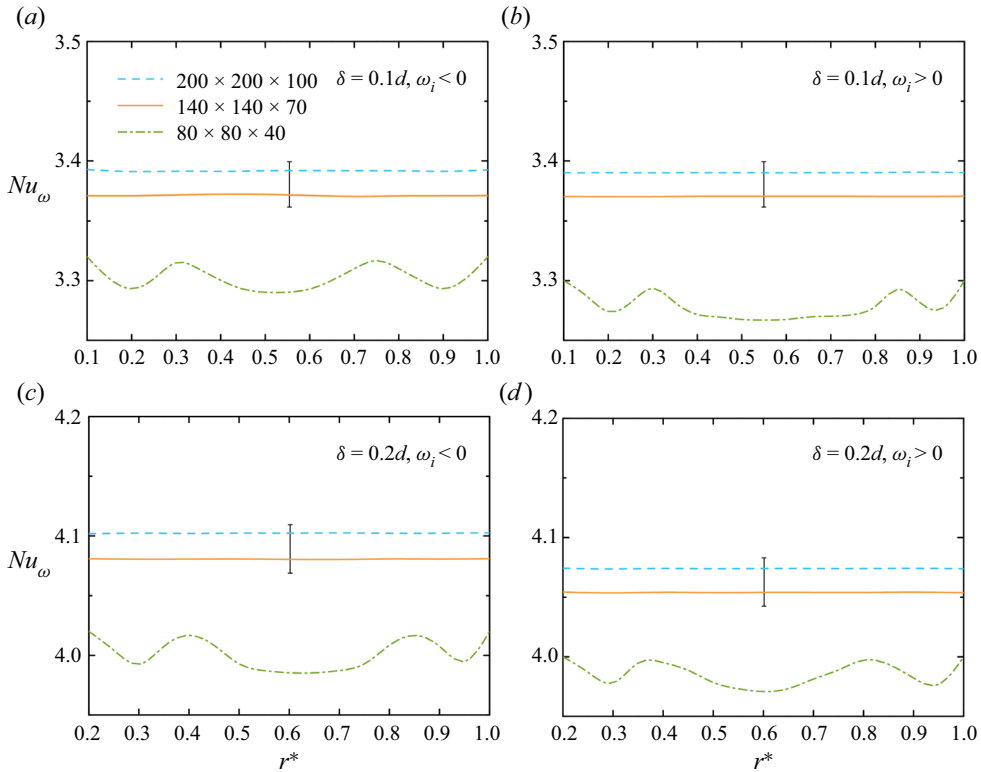
Figure 11. Radial dependence of Nu_ω for different strip heights and different rotating directions of inner rough wall at $Ta = 2.44 \times 10^5$ with three different grid resolutions. An error bar indicating a 1 % error is provided for reference, the resolved cases lie within this error bar.

Author ORCIDs.

Chao Sun https://orcid.org/0000-0002-0930-6343;

Junwu Wang https://orcid.org/0000-0003-3988-1477.

Appendix A. Resolution tests and numerical details

To obtain reliable numerical results, the grid's spatial resolutions have to be sufficient. The requirements for spatial resolution is to have the grid length in each direction of the order of local Kolmogorov length. In the present simulations, the hexahedral grid was uniform in the azimuthal and axial directions, and refined near the inner and outer cylindrical walls in the radial direction (Dong 2007; Ostilla-Mónico *et al.* 2013). In TC flow, J^ω and $Nu_\omega = J^\omega/J^\omega_{lam}$ should not be a function of the radius as mentioned previously, but numerically it does show some dependence. Because of numerical error, J^ω will deviate slightly along the r from a fixed value. To quantify this difference, Zhu *et al.* (2016) defined

$$\Delta_J = \frac{\max(J^\omega(r)) - \min(J^\omega(r))}{\langle J^\omega(r) \rangle_r}, \tag{A1}$$

where the maximum and minimum values are determined over all r, which is selected to be within the scope of $r_i + \delta \leq r \leq r_o$. It is a very strict requirement for the meshes that $\Delta_J \leq 0.01$ (Ostilla-Mónico *et al.* 2013). We make sure all the simulations meet this criterion, the details are listed in table 1.

A resolution test of grid length has been exemplified in figure 11, which presents four graphs of radial dependence of Nu_ω for different strip heights and different rotating directions of the inner rough wall at $Ta = 2.44 \times 10^5$ with three different grid resolutions. An error bar indicating a 1 % error is provided for reference. It is shown that for the under-resolved cases ($N_\varphi \times N_r \times N_z = 80 \times 80 \times 40$), the error of the Nu_ω along the radius is larger than 1 %. However, the Nu_ω error is less than 1 % for the reasonably resolved cases ($N_\varphi \times N_r \times N_z = 140 \times 140 \times 70$) and the extremely well-resolved cases ($N_\varphi \times N_r \times N_z = 200 \times 200 \times 100$).

REFERENCES

BAKHUIS, D., EZETA, R., BERGHOUT, P., BULLEE, P.A., TAI, D., CHUNG, D., VERZICCO, R., LOHSE, D., HUISMAN, S.G. & SUN, C. 2020 Controlling secondary flow in Taylor–Couette turbulence through spanwise-varying roughness. *J. Fluid Mech.* **883**, A15.

BERGHOUT, P., BULLEE, P.A., FUCHS, T., SCHARNOWSKI, S., KÄHLER, C.J., CHUNG, D., LOHSE, D. & HUISMAN, S.G. 2021 Characterizing the turbulent drag properties of rough surfaces with a Taylor–Couette set-up. *J. Fluid Mech.* **919**, A45.

BERGHOUT, P., ZHU, X., CHUNG, D., VERZICCO, R., STEVENS, R.J.A.M. & LOHSE, D. 2019 Direct numerical simulations of Taylor–Couette turbulence: the effects of sand grain roughness. *J. Fluid Mech.* **873**, 260–286.

BRAUCKMANN, H.J. & ECKHARDT, B. 2013 Direct numerical simulations of local and global torque in Taylor–Couette flow up to $Re = 30\,000$. *J. Fluid Mech.* **718**, 398–427.

CADOT, O., COUDER, Y., DAERR, A., DOUADY, S. & TSINOBER, A. 1997 Energy injection in closed turbulent flows: stirring through boundary layers versus inertial stirring. *Phys. Rev.* E **56** (1), 427–433.

CHAN, L., MACDONALD, M., CHUNG, D., HUTCHINS, N. & OOI, A. 2018 Secondary motion in turbulent pipe flow with three-dimensional roughness. *J. Fluid Mech.* **854**, 5–33.

CHUNG, D., HUTCHINS, N., SCHULTZ, M.P. & FLACK, K.A. 2021 Predicting the drag of rough surfaces. *Annu. Rev. Fluid Mech.* **53**, 439–471.

DONG, S. 2007 Direct numerical simulation of turbulent Taylor–Couette flow. *J. Fluid Mech.* **587**, 373–393.

ECKHARDT, B., GROSSMANN, S. & LOHSE, D. 2007 Torque scaling in turbulent Taylor–Couette flow between independently rotating cylinders. *J. Fluid Mech.* **581**, 221–250.

FLACK, K.A. & SCHULTZ, M.P. 2014 Roughness effects on wall-bounded turbulent flows. *Phys. Fluids* **26** (10), 101305.

GROSSMANN, S., LOHSE, D. & SUN, C. 2016 High–Reynolds number Taylor–Couette turbulence. *Annu. Rev. Fluid Mech.* **48**, 53–80.

JELLY, T.O., RAMANI, A., NUGROHO, B., HUTCHINS, N. & BUSSE, A. 2022 Impact of spanwise effective slope upon rough-wall turbulent channel flow. *J. Fluid Mech.* **951**, A1.

LEE, S.-H., CHUNG, H.-T., PARK, C.-W. & KIM, H.-B. 2009 Experimental investigation of the effect of axial wall slits on Taylor–Couette flow. *Fluid. Dyn. Res.* **41** (4), 045502.

MA, G.-Z., XU, C.-X., SUNG, H.J. & HUANG, W.-X. 2020 Scaling of rough-wall turbulence by the roughness height and steepness. *J. Fluid Mech.* **900**, R7.

MODESTI, D., ENDRIKAT, S., HUTCHINS, N. & CHUNG, D. 2021 Dispersive stresses in turbulent flow over riblets. *J. Fluid Mech.* **917**, A55.

MOTOZAWA, M., ITO, T., IWAMOTO, K., KAWASHIMA, H., ANDO, H., SENDA, T., TSUJI, Y. & KAWAGUCHI, Y. 2013 Experimental investigations on frictional resistance and velocity distribution of rough wall with regularly distributed triangular ribs. *Intl J. Heat Fluid Flow* **41**, 112–121.

NG, J.H., JAIMAN, R.K. & LIM, T.T. 2018 Interaction dynamics of longitudinal corrugations in Taylor–Couette flows. *Phys. Fluids* **30** (9), 093601.

NIKURADSE, J. 1933 Stromungsgesetze in rauhen Rohren. *Forschungsheft Arb. Ing.-Wes.* **361**.

OSTILLA-MÓNICO, R., STEVENS, R.J.A.M., GROSSMANN, S., VERZICCO, R. & LOHSE, D. 2013 Optimal Taylor–Couette flow: direct numerical simulations. *J. Fluid Mech.* **719**, 14–46.

OSTILLA-MÓNICO, R., VAN DER POEL, E.P., VERZICCO, R., GROSSMANN, S. & LOHSE, D. 2014*a* Exploring the phase diagram of fully turbulent Taylor–Couette flow. *J. Fluid Mech.* **761**, 1–26.

OSTILLA-MÓNICO, R., VERZICCO, R., GROSSMANN, S. & LOHSE, D. 2014*b* Turbulence decay towards the linearly stable regime of Taylor–Couette flow. *J. Fluid Mech.* **748**, R3.

OSTILLA-MÓNICO, R., VERZICCO, R. & LOHSE, D. 2015 Effects of the computational domain size on direct numerical simulations of Taylor–Couette turbulence with stationary outer cylinder. *Phys. Fluids* **27** (2), 025110.

PIRRO, D. & QUADRIO, M. 2008 Direct numerical simulation of turbulent Taylor–Couette flow. *Eur. J. Mech. (B/Fluids)* **27** (5), 552–566.

POPE, S.B. 2000 *Turbulent Flows*. Cambridge University Press.

RAZZAK, MD.A., CHEONG, K.B. & LUA, K.B. 2020 Numerical study of Taylor–Couette flow with longitudinal corrugated surface. *Phys. Fluids* **32** (5), 053606.

ROUHI, A., CHUNG, D. & HUTCHINS, N. 2019 Direct numerical simulation of open-channel flow over smooth-to-rough and rough-to-smooth step changes. *J. Fluid Mech.* **866**, 450–486.

SHEN, Y., TONG, P. & XIA, K.-Q. 1996 Turbulent convection over rough surfaces. *Phys. Rev. Lett.* **76** (6), 908.

SODJAVI, K., RAVELET, F. & BAKIR, F. 2018 Effects of axial rectangular groove on turbulent Taylor–Couette flow from analysis of experimental data. *Exp. Therm. Fluid Sci.* **97**, 270–278.

STRINGANO, G., PASCAZIO, G. & VERZICCO, R. 2006 Turbulent thermal convection over grooved plates. *J. Fluid Mech.* **557**, 307–336.

VAN DEN BERG, T.H, DOERING, C.R., LOHSE, D. & LATHROP, D.P. 2003 Smooth and rough boundaries in turbulent Taylor–Couette flow. *Phys. Rev.* E **68** (3), 036307.

VERSCHOOF, R.A., ZHU, X., BAKHUIS, D., HUISMAN, S.G., VERZICCO, R., SUN, C. & LOHSE, D. 2018 Rough-wall turbulent Taylor–Couette flow: the effect of the rib height. *Eur. Phys. J.* E **41** (10), 1–9.

WHITE, F.M. 2011 *Fluid Mechanics*. McGraw-Hill.

XU, B., LI, H., LIU, X., XIANG, Y., LV, P., TAN, X., ZHAO, Y., SUN, C. & DUAN, H. 2023 Effect of micro-grooves on drag reduction in Taylor–Couette flow. *Phys. Fluids* **35** (4), 043608.

XU, F., ZHAO, P., SUN, C., HE, Y. & WANG, J. 2022 Direct numerical simulation of Taylor–Couette flow: regime-dependent role of axial walls. *Chem. Engng Sci.* **263**, 118075.

ZHAO, P., XU, J., GE, W. & WANG, J. 2020*a* A CFD-DEM-IBM method for Cartesian grid simulation of gas-solid flow in complex geometries. *Chem. Engng J.* **389**, 124343.

ZHAO, P., XU, J., LIU, X, GE, W. & WANG, J. 2020*b* A computational fluid dynamics-discrete element-immersed boundary method for Cartesian grid simulation of heat transfer in compressible gas–solid flow with complex geometries. *Phys. Fluids* **32** (10), 103306.

ZHU, B., JI, Z., LOU, Z. & QIAN, P. 2018*a* Torque scaling in small-gap Taylor–Couette flow with smooth or grooved wall. *Phys. Rev.* E **97** (3), 033110.

ZHU, X., OSTILLA-MÓNICO, R., VERZICCO, R. & LOHSE, D. 2016 Direct numerical simulation of Taylor–Couette flow with grooved walls: torque scaling and flow structure. *J. Fluid Mech.* **794**, 746–774.

ZHU, X., VERSCHOOF, R.A., BAKHUIS, D., HUISMAN, S.G., VERZICCO, R., SUN, C. & LOHSE, D. 2018*b* Wall roughness induces asymptotic ultimate turbulence. *Nat. Phys.* **14** (4), 417–423.

ZHU, X., VERZICCO, R. & LOHSE, D. 2017 Disentangling the origins of torque enhancement through wall roughness in Taylor–Couette turbulence. *J. Fluid Mech.* **812**, 279–293.